Velocity profiles, stresses, and Bagnold scaling of sheared granular system in zero gravity

Oleh Baran[a] and Lou Kondic[b]
Department of Mathematical Sciences and Center for Applied Mathematics and Statistics, New Jersey Institute of Technology, Newark, New Jersey 07102

(Received 28 July 2004; accepted 19 May 2005; published online 29 June 2005)

We report the results of three-dimensional event-driven simulations of sheared granular system in a Couette geometry. The simulations use realistic boundary conditions that may be expected in physical experiments. For a range of boundary properties we report velocity and density profiles, as well as forces on the boundaries. In particular, we find that the results for the velocity profiles throughout the shearing cell depend strongly on the interaction of the system particles with the physical boundaries. Even frictional boundaries can allow for significant slippage of the particles, therefore reducing the shear in the system. Next, we present stress distributions both for controlled volume and for controlled stress configurations. We discuss the dependence of solid volume fraction on shear rate under the constant-pressure condition, and Bagnold scaling in volume-controlled simulations. In addition, we study the influence of oscillatory driving of one of the domain boundaries on the system properties. © *2005 American Institute of Physics*.
[DOI: 10.1063/1.1951567]

I. INTRODUCTION

Sheared granular flows are important for both the better understanding of the physics of granular matter and in many industrial applications (mixing, transport, etc.). A significant progress in the area of sheared granular systems has been made for the particular flows with simplified boundary conditions on the theoretical,[1,2] numerical,[3,4] and experimental[5] levels. The simplifications used in these studies often involve simplifying or ignoring the effect of physical boundaries (as with periodic boundary conditions), and assuming approximately constant volume fraction throughout the system.

However, for applications it is important to understand the effect of realistic boundaries on the sheared granular flow. There has been a number of studies that addressed this problem. Jenkins and Richman,[6] for example, calculated boundary conditions in a specific limit of plane flow of identical, smooth, inelastic disks interacting with a bumpy wall. Louge, Jenkins, and Hopkins[7] and later Louge[8] tested these theoretical predictions for rapid sheared granular flows using computer simulations. Related approaches to the question of boundary conditions in continuum theories have been made by Hui *et al.*[9] and Gutt and Haff.[10] Alam and Nott[11] and Nott *et al.*[12] theoretically studied the effect of boundaries on the stability of plane Couette flow of granular materials. In this work, we build upon these previous works and use discrete element simulations to perform a systematic study of the effect of realistic boundary conditions on sheared granular flow in a three-dimensional (3D) Couette cell under zero gravity.

The paper is organized as follows. Section II describes the numerical approach and relevant parameters for our hard sphere (event-driven) simulations. In Sec. III we present the results for bulk velocity and volume fraction profiles for a variety of boundary conditions. We also consider granular systems which are, in addition to shear, subject to excitations provided by an oscillatory boundary. These oscillations are shown to lead to considerable modifications of velocity and volume fraction profiles. In Sec. IV we discuss stresses on the physical boundaries. In contrast to other works (most notably Ref. 8), we do not analyze in detail how changes of the boundary conditions influence the system response, but instead concentrate on the stress distributions for given boundary conditions. We compare the normal and shear components of the stresses and discuss the factors determining the widths of the distributions and their average values, with particular emphasis on the issues related to measuring stresses in granular system characterized by moderate to high volume fractions.

All the results in Secs. III and IV are obtained for the systems of directly controlled total volume. In Sec. V we present the stresses, velocities, and volume fraction profiles under stress-controlled conditions. We then discuss the differences between these two configurations.

II. SIMULATION DETAILS

Numerical algorithm of our choice, event-driven algorithm for hard spheres, is described in detail in the papers by Lubachevsky[13] and Luding.[14] In zero gravity all particles follow linear trajectories between the collisions. All collisions between particles are instantaneous and binary. Consider two colliding particles with diameters σ_1 and σ_2, masses m_1 and m_2, positions $\mathbf{r}_1$ and $\mathbf{r}_2$, linear and angular velocities $\mathbf{v}_1$, $\boldsymbol{\omega}_1$ and $\mathbf{v}_2$, $\boldsymbol{\omega}_2$. Then velocities after collision are

[a]Present address: ExxonMobil Research and Engineering, 1545 Route 22 East, Annandale, NJ 08801. Electronic mail: oleh.baran@exxonmobil.com
[b]Author to whom correspondence should be addressed. Electronic mail: kondic@njit.edu

TABLE I. Typical choice of dissipation parameters.

Particles (including glued)	$\epsilon=0.6$	$\mu=0.5$	$\beta_0=0.35$	Frictional inelastic particles
Top and bottom walls	$\epsilon_w=0.1$	$\mu_w=0.9$	$\beta_{0w}=0.35$	Very frictional and inelastic
Sidewalls	$\epsilon_s=0.9$	$\mu_s=0.1$	$\beta_{0s}=0.35$	Slightly frictional and inelastic

$$\mathbf{v}_1' = \mathbf{v}_1 - \frac{m_2}{m_1+m_2}\Delta\mathbf{V}, \quad \mathbf{v}_2' = \mathbf{v}_2 + \frac{m_1}{m_1+m_2}\Delta\mathbf{V}; \tag{1}$$

$$\boldsymbol{\omega}_1' = \boldsymbol{\omega}_1 + \frac{m_2}{m_1+m_2}\frac{\Delta\mathbf{W}}{\sigma_1}, \quad \boldsymbol{\omega}_2' = \boldsymbol{\omega}_2 + \frac{m_1}{m_1+m_2}\frac{\Delta\mathbf{W}}{\sigma_2}; \tag{2}$$

where

$$\Delta\mathbf{V} = (1+e)\mathbf{v}_n + \tfrac{2}{7}(1+\beta)\mathbf{v}_t, \quad \Delta\mathbf{W} = \tfrac{10}{7}(1+\beta)[\mathbf{n}\times\mathbf{v}_t]. \tag{3}$$

Here $\mathbf{n}=(\mathbf{r}_1-\mathbf{r}_2)/|\mathbf{r}_1-\mathbf{r}_2|$ is the normal unit vector, $\mathbf{v}_n$ and $\mathbf{v}_t$ are the normal and tangential components of the relative velocity $\mathbf{v}_c=\mathbf{v}_1-\mathbf{v}_2-\left[\left(\frac{1}{2}\sigma_1\boldsymbol{\omega}_1+\frac{1}{2}\sigma_2\boldsymbol{\omega}_2\right)\times\mathbf{n}\right]$ of particles at the contact point. Total linear and angular momentums are conserved during a collision; however, total translational and rotational energies are lost.

Energy dissipation is controlled by three parameters:[15] the coefficient of restitution e, coefficient of friction μ, and coefficient of tangential restitution β. The algorithm is adapted to include the particle's interaction with physical boundaries in the following way. The collisions with the top or bottom walls (also called horizontal walls) assume that a wall is a particle of infinite radius and mass, and of linear velocity equal to the wall's velocity at the point of contact. Three dissipation parameters, e_w, μ_w, and β_w, characterize these collisions. The sidewalls are the particles of infinite mass and radius and with the surface normal pointing horizontally toward the center of the cell. The properties of the sidewalls are characterized by a separate set of parameters, e_s, μ_s, and β_s.

Experiments and theoretical studies show that the coefficient of restitution e noticeably depends on the impact velocity.[16,17] Therefore, we set this coefficient to be velocity dependent in the manner suggested in Ref. 18

$$e(v_n) = \begin{cases} 1 - Bv_n^{3/4}, & v_n < v_0, \\ \epsilon, & v_n > v_0. \end{cases} \tag{4}$$

Here v_n is the component of relative velocity along the line joining particle centers, $B=(1-\epsilon)v_0^{(-3/4)}$, $v_0=100\langle d\rangle/\mathrm{sec}$, and ϵ is a restitution parameter.

Coefficient of tangential restitution β, defined as the ratio of the tangential components of the relative velocity after and before collision, is given by[14,18,19]

$$\beta = \begin{cases} -1 + \frac{7}{2}\mu(1+e)v_n/v_t & \text{for sliding contacts,} \\ \beta_0 & \text{for rolling contacts.} \end{cases} \tag{5}$$

Here μ is the coefficient of friction, e is given by (4), and β_0 determines the transition between rolling and sliding contacts.[14,19]

Table I summarizes our choice of dissipation parameters for typical configurations. When different dissipation parameters are used in the simulations, the results are always compared to the typical configuration.

Figure 1 shows the geometry of our 3D simulations of polydisperse inelastic frictional spheres in the Couette cell, with stationary sidewalls, rotated top wall, and the bottom wall that can move in the vertical direction. This feature allows us to, e.g., oscillate the bottom wall, similar to the laboratory experiments.[20] In addition, the moving bottom wall is used in stress-controlled simulations, where granular particles determine the position of the bottom wall on their own. More details can be found in Sec. V.

The particles are polydisperse with diameters randomly distributed in the range $[0.9,1.1]\langle d\rangle$, where $\langle d\rangle$ is the average diameter of particles, which is used as a natural length scale. Our typical configuration consist of $N=2000$ particles, with fixed radii of inner cylinder and outer cylinder ($R_i=8\langle d\rangle, R_o=12\langle d\rangle$). The height H of the cell is variable and depends on the volume fraction ν, or on the average stress. For example, in the case of volume-controlled simulations with 40% volume fraction, we have $H(\nu,t)=[4.22/\nu+A\sin(2\pi ft)]\langle d\rangle$. Here A and f are the amplitude scaled by $\langle d\rangle$, and the frequency in hertz of the bottom wall vibrations, if any. Typically we use $A=1\langle d\rangle$ and $f_t=36.6$ Hz, giving the dimensionless parameter $\Gamma=A(2\pi f)^2/g$, which is above critical for the onset of fluidization. Another system size briefly studied is a *wide configuration* that has $N=5000$ particles in a Couette cell with radii of inner and outer cylinders $R_i=5\langle d\rangle$ and $R_o=15\langle d\rangle$, respectively. This configuration is used to show 3D nature of the results.

The top wall can be covered with particles glued to its

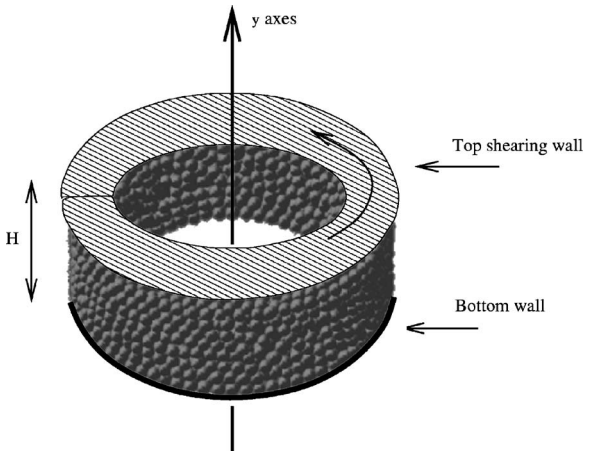

FIG. 1. Granular matter between two concentric stationary cylinders—sidewalls (not shown in the figure). Top wall is rotating around the vertical y axes. Bottom wall can be vibrated in volume-controlled simulations, or it can move as a result of applied stress in pressure-controlled simulations.

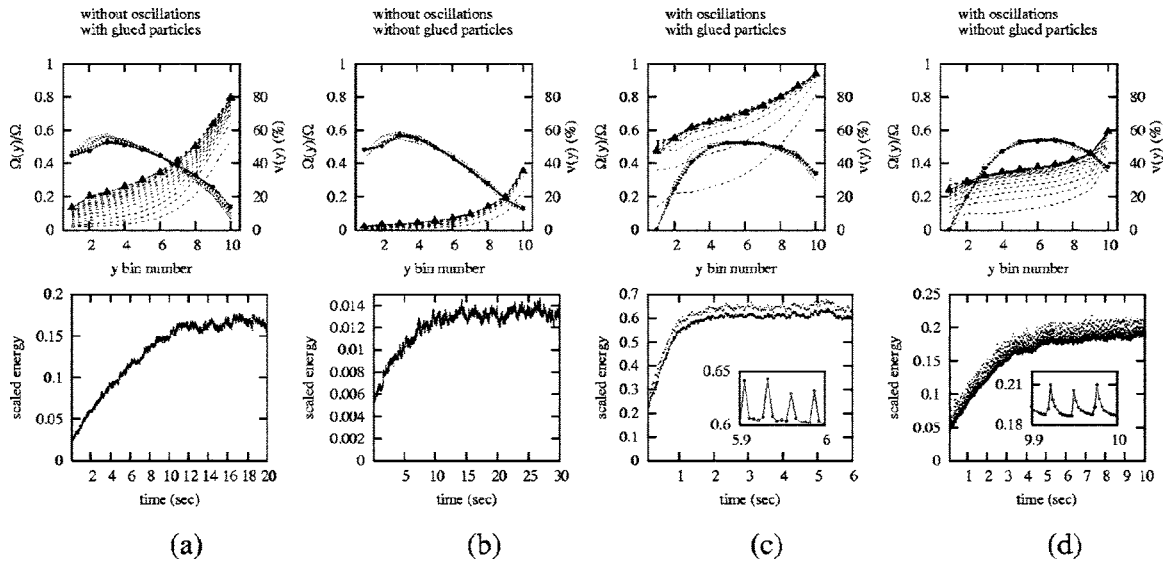

FIG. 2. Typical configurations results. Top panel: scaled velocity profiles (triangles) and volume fraction profiles (circles) in steady-state regime together with the profiles in transient regimes (dashed lines). Bottom panel: scaled energy plots. Insets in energy plots: kinetic energy plotted on a shorter time scale showing the frequency of bottom wall oscillations. (a) and (b) Results without oscillating bottom wall; (c) and (d) with oscillations; (a) and (c) shearing wall with glued particles; (b) and (d) without glued particles. The dissipation parameters are as shown in Table I.

surface, which have the same polydispersity, mean diameter, and material properties as the free particles. They are glued into the dimples on the surface so that each one protrudes inside the cell by the distance of half its diameter. For both typical and wide configurations, the number of glued particles corresponds to $\approx 30\%$ surface fraction, leading to configurations such that on average free particles cannot reach the flat wall. The relevance of the distance between glued particles as a measure of surface roughness is discussed in Ref. 6.

The initial conditions are prepared by first positioning N particles inside the container of the extended vertical dimension with large initial spacing between the particles. Initially, particles and walls are set to be completely elastic and frictionless. The particles are assigned random velocities, and the bottom is then moved up slowly until the desired volume fraction is reached. The resulting sample is then run for a longer time to eliminate compression waves (if any) created by compression. The total momentum is then adjusted to zero, and finally the particles are set to be inelastic and frictional (see Table I).

III. VELOCITY AND VOLUME FRACTION PROFILES

To measure angular velocity and volume fraction profiles, $\Omega(y)$ and $\nu(y)$, respectively, the volume of Couette cell is divided in N_s ring slices. Each slice is assigned a y bin number $i_y = 1, \ldots, N_s$. In most cases, we set $N_s = 10$. When the bottom wall is oscillated, we account for variable volume of the bottom slice or slices. In our measurements we average a studied quantity both over the volume of a y bin and over the time interval t_p, typically $t_p = 0.5$ sec. Within this time interval we measure the particle's velocities and ν's every δt_p leading to $N_p = t_p / \delta t_p$ different distributions. It is convenient to express time in terms of $T_w = 1/f_t$, giving $t_p = 18.3 T_w$; we use $\delta t_p = T_w / 10$. All particles are binned in the corresponding ring slices, and the average ν and the average velocity are calculated as a function of y bin number. For wide configurations, in addition we measure ν as a function of the distance to the inner cylinder, $\nu(r)$.

A. Configurations with inelastic and frictional sidewalls

Figure 2 shows the velocity profiles (top) and scaled total kinetic energy (bottom). The latter is the kinetic energy per particle scaled by the energy of a particle of average diameter and of average linear top wall velocity. All the measurements are done for the typical configuration systems with 2000 particles and in zero gravity, but with four different boundary conditions: (a) and (b) without oscillating bottom wall; (c) and (d) with oscillations; (a) and (c) shearing wall with glued particles; (b) and (d) without glued particles. When oscillations are present, the position of the bottom wall is given by $y = A \sin(2\pi f t)$, with $A = \langle d \rangle$ and $f = f_t = 36.6$ Hz. In all four cases the shearing wall is rotating with $\Omega = 10$ rad/sec. This sets the linear shearing velocity range between 80 $\langle d \rangle$/sec (close to inner cylinder) and 120 $\langle d \rangle$/sec (close to outer cylinder). The effect of different shearing velocities is discussed later in this section.

Figure 2(a) shows that in the case of glued particles on the top wall, and no oscillations, the system reaches a state characterized by a significant shear throughout the domain. By comparing 2(a) and 2(b), we see that there is a strong effect of glued particles on increasing shear. We emphasize that the top wall without glued particles, Fig. 2(b), does not lead to significant shear, although the wall itself is very frictional and inelastic. Also, we note that our simulations lead to asymmetric volume fraction distribution with significant dilation close to the shearing surface, in contrast to, e.g., Ref. 7 which shows symmetric volume fraction profiles. The symmetry in our system is broken due to the presence of (sta-

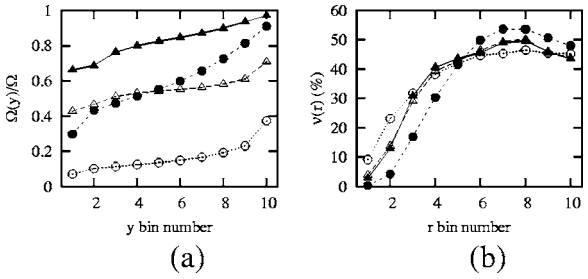

FIG. 3. Results for wide configurations: with glued particles and oscillations (filled triangles); without glued particles and with oscillations (open triangles); with glued particles and without oscillations (filled circles); without glued particles and without oscillations (open circles). (a) Velocity profiles in the y direction. (b) Volume fraction profiles in the radial direction.

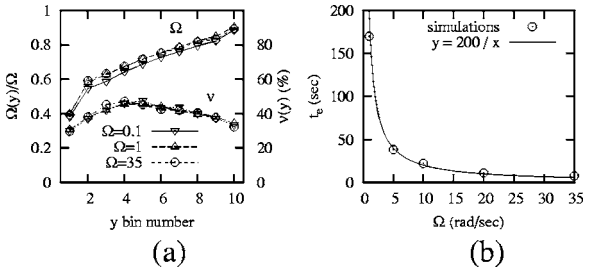

FIG. 4. (a) Linear-asymmetric velocities and ν's for the case of elastic sidewalls, no glued particles, and no oscillations. (b) Equilibrating times t_e.

tionary) sidewalls, due to the glued particles being present only at the the top wall, and by other effects, such as velocity-dependent restitution coefficient, see (4).

Figures 2(c) and 2(d) show the results with oscillations, which account for a considerable slip velocity at the bottom wall. Similar to the case without oscillations, the presence of glued particles greatly reduces the slip velocity at the top wall. We note that our results are in agreement with the ones derived using kinetic theory with simplified interaction model between the free particles and the walls,[6,9] which predict that slip velocity is inversely proportional to some measure of roughness, and directly proportional to the local shear rate. The influence of roughness is clear from the results obtained with and without glued particles. By direct comparison, we also verify that larger local shear rate in the system without oscillations, shown in Fig. 2(a), results in larger slip velocity.

Figure 2 also shows ν as a function of y. The steady states, marked by the circles, show that ν's are not uniform, in contrast to volume fraction profiles typically obtained under the assumption of periodic boundary conditions. For each of four cases we observe the maximum local $\nu \approx 58\%$ for some intermediate y's, with dilation effects close to the walls. Oscillations, in particular, lead to very small ν's close to the bottom wall. This is due to the fact that when the bottom wall moves downward, the adjacent granular layer does not follow it. This is also confirmed by computer visualization of the granular layer.

From energy plots, shown in the bottom panel of Fig. 2, we estimate the equilibrating time needed to reach steady state for all four cases: $t_e(a)=15$ sec, $t_e(b)=15$ sec, $t_e(c)=2$ sec, and $t_e(d)=6$ sec. These times are shorter for the systems with oscillating bottom wall due to increased collision rate. Also, oscillations lead to modulation of the scaled energy; this is shown in the insets in the energy plots. In addition, in the systems with oscillations, the glued particles provide an increase in collision rate and decrease in equilibration time.

Figure 3 shows the velocities and ν's for wide configuration, characterized by 5000 particles, and $\nu=40\%$, using typical values of all other parameters. The velocity profiles, shown in Fig. 3(a), are qualitatively similar to the ones shown in Fig. 2, although velocities are slightly larger for wide configuration, since the ratio of the areas of dissipative sidewalls to the area of shearing wall is smaller. The ν's (not shown) are very similar to those in Fig. 2.

Figure 3(b) shows $\nu(r)$. We see that there is a significant dilation near the inner wall due to centrifugal effect, since the particles colliding with the top wall gain the momentum that, on average, has a direction along the tangent line to the trajectory at the contact point. On the other hand, the dependence of particle velocities on r (not shown) is rather weak.

B. Effect of dissipation parameters and shearing velocity without oscillations

Here, as a basis, we use $\nu=40\%$ typical configuration without oscillations and without glued particles [Fig. 2(b)], with one modification: to enhance shear, we assume completely elastic sidewalls.

Figure 4(a) shows that there is a significant, qualitative difference of the velocity profiles for the systems with elastic and smooth sidewalls compared to inelastic and rough sidewalls shown in Fig. 2(b). Effect of shearing is much stronger in the systems with elastic sidewalls, with almost linear velocity profile and large slippage at the bottom. We refer to this shape of velocity profile as *linear asymmetric*, and note that if we shear the same initial configuration by rotating the top wall in one direction and bottom wall in the opposite one, we obtain *linear-symmetric* velocity profile with equal slippage at the top and bottom.

Figure 4(a) shows that the velocity and volume fraction profiles are very similar as Ω's are varied over more than two orders of magnitude. The energy plots similar to the ones shown in Fig. 2 show, however, that the time to reach the steady state (*equilibrating time*), t_e, does depend strongly on Ω. This effect is shown in more detail in Fig. 4(b), which shows that t_e is inversely proportional to Ω. Therefore, the same amount of strain is needed to reach the steady state for all explored shearing velocities. We note that in our simulations we do not observe instabilities of layering type,[11,12] possibly due to relatively small height of our computational domain.

In the next set of simulations we investigate the effect of horizontal walls properties in the same system. Out of three parameters that characterize the horizontal walls $(\epsilon_w, \beta_{0w}, \mu_w)$, we vary one at a time and keep the others fixed. We find that ϵ_w and β_{0w} have relatively weak effect on the velocity profiles. However, μ_w influences the flow strongly. There exists a critical value μ_w^c, below which the

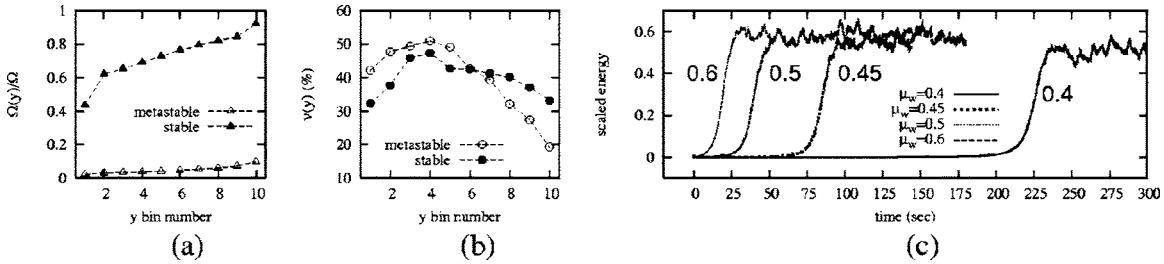

FIG. 5. Delayed dynamics regime. The shearing velocity in all cases is $\Omega=10$ rad/sec. (a) and (b) show the typical velocity and volume fraction profiles in metastable and stable states, using $\mu_w=0.45$ at $t=30$ sec (metastable state) and $t=150$ sec (stable state). (c) Scaled energy as a function of time for four values of μ_w.

frictional force from the shearing wall cannot excite the granular flow. For our configuration this value is $\mu_w^c \lesssim 0.4$. Understanding precisely the role of μ_w requires careful analysis, and we devote the rest of this section to this aspect of the problem.

Figure 5, which presents the results for μ_w in the interval [0.4, 0.9], shows that the systems first reach a metastable state of slow shearing [open symbols in Figs. 5(a) and 5(b)]. This metastable state is characterized by negligibly small slippage at the bottom wall and very large slippage at the top, as well as by high ν close to the bottom. As time progresses, the shear of the granular particles is increasing very slowly. However, after certain time t_c, the system jumps into a stable state of fast shearing with asymmetric-linear profile, also shown in Figs. 5(a) and 5(b). We call this behavior *delayed dynamics*. This jump from metastable to stable state is illustrated in Fig. 5(c), which shows the scaled energy (kinetic energy per particle scaled by the energy of a particle of average diameter and of average linear top wall velocity) for four values of μ_w.

Figure 6(a) shows the crossover *transition time* t_c, defined as the time when metastable state ends, i.e., when the granular layer starts to pick up the energy fast. We find that $t_c \sim (\mu_w - \mu_w^c)^{-2}$, with critical friction parameter $\mu_w^c=0.33$. Figure 6(b), which shows scaled energy for $\mu_w=0.4$, illustrates the manner in which t_c is obtained. The intersection of the tangent lines and the time axis gives t_c, and the intersection with the horizontal line at the level of the average scaled energy in the steady state gives equilibrating time t_e. For all considered μ_w's, $\delta t_e = t_e - t_c$ is $\approx(18\pm4)$ sec. This result is consistent with t_e obtained for the same $\Omega=10$ rad/sec and very frictional horizontal walls ($\mu_w=0.9$), see Fig. 4(b). For such a large μ_w, $t_c \approx 0$, and $\delta t_e \approx t_e$.

Figure 7(a) illustrates the effect of Ω for the system in delayed dynamics regime for three different shearing velocities, confirming that the transition times t_c depend very weakly on Ω. However, the δt_e's follow the inverse rule shown in Fig. 4(b). Therefore, δt_e's strongly depend on Ω, while being almost independent of μ_w.

To understand precisely the role which the horizontal walls play in the mechanism of delayed dynamics, we now consider fixed coefficient of friction of the top wall $\mu_w(\text{top})=0.45$ and vary coefficient of friction of the bottom wall. The results, shown in Fig. 7(b), clearly indicate that μ_w(bottom) does not have important effect on t_c. However, smaller μ_w(bottom) leads to shorter δt_e. We also note that for these low μ_w(bottom) the energies are rising to the higher values. This is an indication of higher overall velocities of the particles in the steady state due to higher slippage at the bottom wall for lower μ_w(bottom).

An insight into the mechanism of the delayed dynamics can be gained by considering also the time dependence of ν's. Recall that Fig. 5(b) indicates formation of a high-density cluster in both metastable and stable states. Figure 8(a) tracks the evolution of this cluster, by showing the position of the center of mass of the particles, $h_{\text{c.m.}} = \Sigma_i d_i^3 y_i / \Sigma_i d_i^3$, scaled by the cell height H, as a function of time. This figure, discussed in more detail below, clearly shows that there is a shift in $h_{\text{c.m.}}$ as system transitions from metastable to stable state [viz. Fig. 5(c) for $\mu_w=0.45$].

Based on the results shown in Figs. 5–8, the mechanism of the delayed dynamics is as follows. The friction of the top

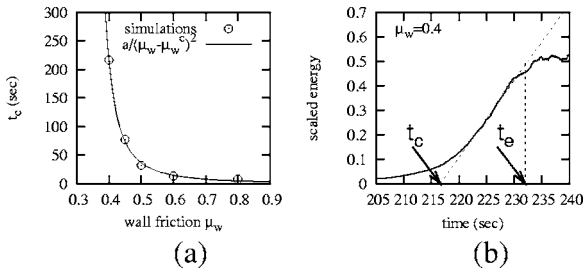

FIG. 6. (a) Transition times t_c vs wall friction: open circles are the simulation results, and the solid line is the best fit using inverse function $t = a/(\mu - \mu_c)^2$ with fitting parameters $a=1.07$ and $\mu_w^c=0.33$. (b) An example of the close-up of "transition interval" for $\mu_w=0.4$. The plot allows to determine the transition time t_c and equilibrating time t_e, as discussed in the text.

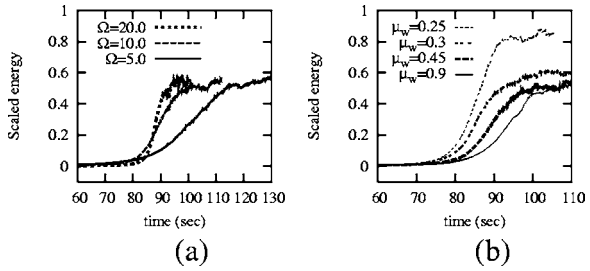

FIG. 7. Scaled energies in the transition interval for (a) $\mu_w=0.45$ with three different shearing velocities, (b) $\mu_w=0.45$ for the top wall, variable μ_w for the bottom wall, $\Omega=10$ rad/sec.

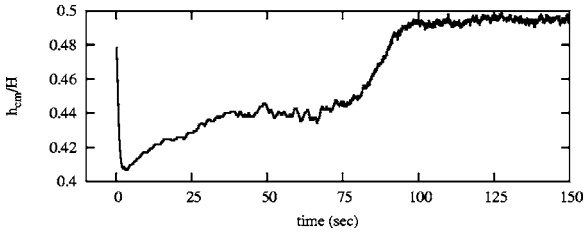

FIG. 8. Scaled center of mass vs time for the system with $\mu_w=0.45$.

wall controls the amount of the tangential momentum transferred to the particles. Thus, the energy input is determined by the top wall friction, as well as by the collision rate with this wall. When the initial configuration is subjected to shear, the particles immediately dilate close to the top wall and form the cluster of high volume fraction close to the bottom wall, see Fig. 8, $t<30$ sec. If the friction of the top wall is weak enough, below some critical value μ_w^c, all the energy is quickly dissipated without inducing any shear. For higher μ_w, the energy transferred to the granular system starts to accumulate slowly, until, at some critical time t_c, the shearing between the dense cluster and the bottom wall is strong enough to dilate a region next to this wall and to push the cluster closer to the top wall, see Fig. 8. This process is accelerated if μ_w(bottom) is smaller. As a result, the collision rate with the top wall increases, and the energy from the top wall is rapidly transferred to the cluster, until the stable state characterized by linear asymmetric profile forms. Thus, the time span of metastable state t_c is determined mostly by the friction of the top wall, and the time δt_e is determined mostly by the shearing velocity.

C. Effects of oscillations

To test the effect of the amplitude A and frequency f of oscillations, it is more convenient to go back to the typical dissipative sidewalls used in Sec. III A, since in the case of smooth sidewalls the slippage velocity at the bottom wall is approaching Ω, making the analysis of the velocity profiles difficult. So, as a base system we use the "oscillating bottom wall, no glued particles" configuration shown in Fig. 2(b).

Figure 9 shows velocity and volume fraction profiles, where (a) f is fixed and A is varied and (b) A is fixed and f is varied. The characteristic feature of these results is high $\nu\approx 50\%-60\%$ in the middle of the cell, confined between two layers of low ν close to the walls. Inside this band the

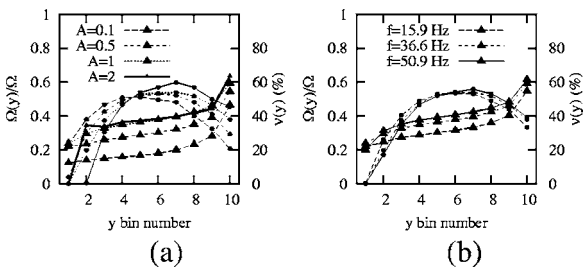

FIG. 9. Velocity (triangles) and volume fractions (circles) for (a) fixed frequency, $f=f_t=36.6$ Hz, and different amplitudes of oscillations; (b) fixed amplitude, $A=\langle d\rangle$, and different f.

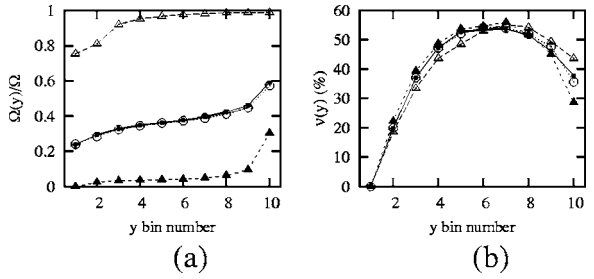

FIG. 10. Effect of sidewall properties on velocities (a) and ν's (b): Typical (filled circles), elastic-smooth (open triangles), very frictional (filled triangles), and elastic-frictional (open circles).

local shear rate is rather low, compared to the overall shear rate. In Fig. 9(a) we observe that the slippage at the bottom wall increases strongly with A. Also, as A increases, the peak of ν profile moves further away from the oscillating wall. Similarly, in Fig. 9(b) we see that an increase of the frequency of oscillations leads to an increase of velocity throughout the system. However, ν's change very little with f.

Figure 10 shows how the properties of sidewalls influence the velocities and ν's. Setting $\mu_s=0$, $\epsilon_s=1$ (Fig. 10, open triangles) makes almost all particles move with Ω. Setting $\mu_s=0.5$, $\epsilon_s=0.6$ (filled triangles) creates already enough dissipation to almost completely resist the shearing force: Even oscillations cannot improve shearing when sidewalls are very frictional. The results for $\mu_s=0.1$, $\epsilon_s=0.6$ (open circles) are almost identical to the results for the typical case, Fig. 2(b) (shown here with filled circles). We conclude that μ_s plays the crucial role in defining velocity profiles, similarly as observed regarding μ_w in Sec. III B. The volume fraction profiles, on the other hand, very weakly depend on the sidewall properties.

IV. NORMAL AND SHEAR STRESSES ON THE BOUNDARIES

Stresses in granular systems have been the focus of many studies, because of their importance in a number of engineering designs. A significant part of these studies[1,21,22] deals with the theoretical continuum models where stress is considered as a mean local quantity. Therefore, the validity of these models depends on the strength of stress fluctuations on the scale which defines "locality." The knowledge of stress distributions becomes crucial here. There are many experimental, numerical, and theoretical studies of stress fluctuations.[23–26] Often, these studies deal with high volume fraction of static or slowly sheared granular systems. In these systems the distribution of stresses is characterized by an exponential decay for large stresses. It is speculated[25] that the exponential tails in stress distributions are related to the presence of force chains. However, recently, Longhi, Easwar, and Menon[27] reported the experimental evidence of exponential tails in stress distributions in rapidly flowing granular medium, i.e., in the systems where it was unlikely to find force chains in the traditional "static" sense.

The results presented in this section concentrate on the stress distributions at the physical boundaries of rapidly

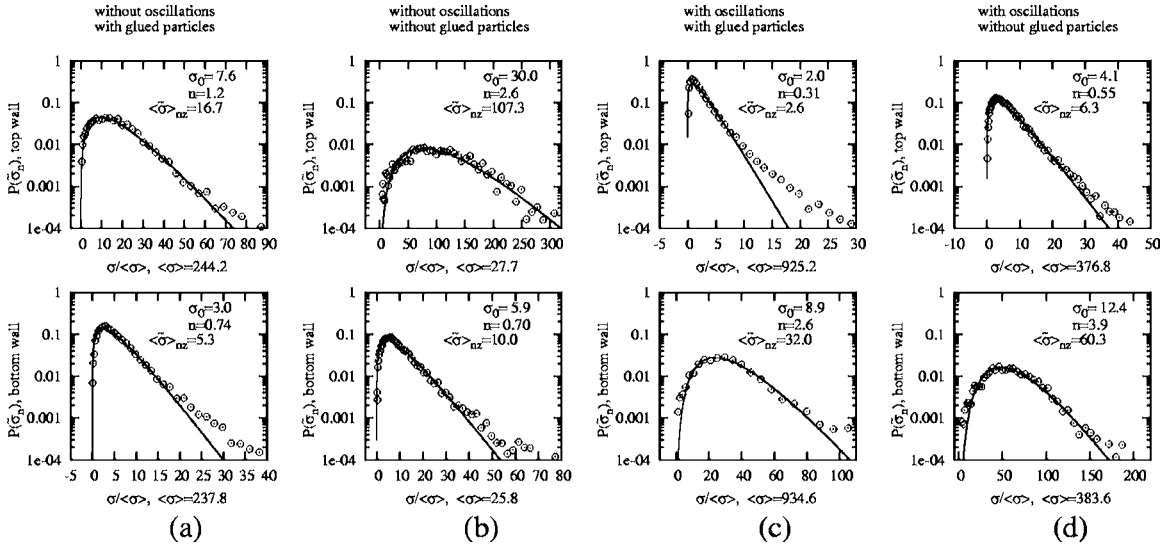

FIG. 11. Log plot of PDF for normal nonzero stresses on the top wall (top panel) and on the bottom wall (bottom panel) in typical configuration with four boundary conditions: (a) and (b) without oscillating bottom wall, (c) and (d) with oscillating bottom wall, (a) and (c) with glued particles, (b) and (d) without glued particles. Average normal stress per area $\langle\sigma\rangle$ is in units of $\rho_s\langle d\rangle^2/\mathrm{sec}^2$. Solid lines: the best fits of the function (9), with the values of the fitting parameter n and corresponding σ_0 and $\langle\sigma\rangle_{nz}$ shown on each plot.

sheared granular systems usually with $\nu=40\%$. In order to make maximum connection with existing experimental results and theories, we calculate the stresses similar to experiments, i.e., we introduce in our simulations stress sensors on the boundaries. For low ν's and/or in rapid flow regime these sensors can report zero stress during some measuring intervals, see, for example, Ref. 27. Therefore, the total distribution of stresses must contain the distribution of *nonzero stresses* and a weighted delta function to account for *zero stresses*. In what follows we make a clear distinction between nonzero and zero stresses and extend all relevant theoretical arguments to account for the latter.

We present the stresses on the boundaries for the typical configurations shown in Fig. 2. To calculate the stresses, we cover the respective boundaries with stress sensors, of the area $A_s=d_s^2$; typically, we set $d_s=1.09\langle d\rangle$ (larger sensors are considered later). We use both square and sector shaped sensors without any difference in the results.

The instantaneous normal and tangential stresses on a sensor are defined as

$$\sigma_n=\frac{\sum_i \Delta p_n(i)}{A_s\Delta t}=\frac{1}{A_s\Delta t}\frac{1}{6}\pi\rho_s\sum_i d_i^3|v_y'-v_y|, \tag{6}$$

$$\sigma_t=\frac{\sum_i \Delta p_t(i)}{A_s\Delta t}=\frac{1}{A_s\Delta t}\frac{1}{6}\pi\rho_s\sum_i d_i^3(v_t'-v_t). \tag{7}$$

Here i counts all the collisions between the particles and the walls in the sensor area during an averaging time interval Δt; typically $\Delta t=T_w/10$. $\Delta p_n(i)$ and $\Delta p_t(i)$ are the changes of particle's normal and tangential momenta, ρ_s is density of the solid material, d_i is the diameter of a particle participating in the collision i, and vectors $\mathbf{v}$ and $\mathbf{v}'$ are the velocities of the colliding particle before and after a collision, respectively. Subscripts n and t refer to the normal and tangential components. To obtain sufficient data for the stress probability distribution function (PDF), we measure instantaneous stresses on all sensors every Δt for at least $\Delta T=1000\Delta t$, and show the scaled PDFs of locally measured stresses, σ_n and σ_t, as a function of $\sigma_n/\langle\sigma_n\rangle$ or $\sigma_t/\langle\sigma_t\rangle$. The averages are defined as

$$\langle\sigma_{(n,t)}\rangle=\left[\sum_i \Delta p_{(n,t)}(i)\right]\Big/ A_{\mathrm{base}}/\Delta T,\quad A_{\mathrm{base}}=\pi(R_o^2-R_i^2). \tag{8}$$

In what follows, we concentrate mostly on the stress distributions and do not discuss in detail the relation between imposed boundary conditions and stresses; more results about this aspect of the problem can be found in the paper by Louge.[8]

A. Normal stress distributions

Figure 11 shows the results for normal nonzero stresses on the top and bottom walls for the same four boundary conditions as in Fig. 2. The main features of the stress distributions are the increase for small stresses and the decrease, in most cases approximately exponential, for large stresses. It is well established experimentally that the exponential tails are the characteristic features of the stress PDFs in *static* granular materials at ν's close to the random close packing.[24,25,28] Although the stresses we measure are not static, nevertheless, the approximately exponential tails are observed in Fig. 11 (except perhaps for very large stresses), as illustrated by the best fit of this functional form

$$P_{nz}(\tilde\sigma)=c\tilde\sigma^n e^{-\tilde\sigma/\sigma_0},\quad \tilde\sigma=\sigma/\langle\sigma\rangle, \tag{9}$$

shown in Fig. 11 as solid lines; we use $\langle\sigma\rangle=\langle\sigma_n\rangle$ as defined in (8). The subscript nz emphasizes that the distributions are built from nonzero stresses. This is important since certain fraction of sensors registers zero stress. Including zero stresses in the definition of P would prevent us from formu-

lating the fitting function (9) and relate our results directly to experiments and theory. We discuss the consequence of this approach in more details below.

The form (9) can be thought of as the generalization of the theoretical predictions for static stress distributions. (The important assumptions of theoretical models of stress distributions are the maintained contact between particles that are closely packed. These assumption are valid in both completely static case and in the case of slow shearing at high density.) For example, the original q model,[26,29] extended later by other authors,[30,31] predicts the distribution (9) with $n=N_c-1$, where N_c is the number of force transmitting contacts between particles in adjacent layers. In 3D and fcc close packing $N_c=3$, so $n=2$. Using different approach, Edwards and Grinev[32] predict the distribution (9) with $n=1/2$. n can also depend on the number of contacts between sensor and particles during averaging time, as will be shown in Sec. IV A 2. Therefore, it makes sense to think of n as a fitting parameter. Other parameters, c and σ_0, can be expressed in terms of n and the average stress $\langle\tilde{\sigma}\rangle_{nz}$ (measured directly in simulations) using the following expressions:

$$1=\int_0^\infty P_{nz}(\tilde{\sigma})d\tilde{\sigma}=c[\Gamma(n+1)\sigma_0^{(1+n)}], \tag{10}$$

$$\langle\tilde{\sigma}\rangle_{nz}=\int_0^\infty \tilde{\sigma}P_{nz}(\tilde{\sigma})d\tilde{\sigma}=\sigma_0(n+1). \tag{11}$$

In Fig. 11 we show the fit of the functional form (9) with n as the only fitting parameter. Other parameters, calculated using (10) and (11), and average quantities, obtained directly from simulations, are also shown. These results show that the average stresses $\langle\sigma\rangle$ at the top and bottom walls are equal within the statistical error. However, the peak values and the widths of distributions are different. In particular, for the systems without oscillations the distributions are wider at the top wall, while if oscillations are present, they are wider at the bottom wall. Before discussing this result, we consider the effects of volume fraction, collision rate, averaging, and correlations on the properties of the stress distributions.

1. The width of stress distributions

Let the width of a distribution be defined as the root mean square of all measured stresses (including zero stresses) divided by the mean stress,

$$\text{width}=\frac{\sqrt{\langle\sigma^2\rangle-\langle\sigma\rangle^2}}{\langle\sigma\rangle}=\frac{\sqrt{\langle\tilde{\sigma}^2\rangle-\langle\tilde{\sigma}\rangle^2}}{\langle\tilde{\sigma}\rangle}=\sqrt{\langle\tilde{\sigma}^2\rangle-1} \tag{12}$$

(here we use $\langle\tilde{\sigma}\rangle=1$, see below). The distribution itself takes the form of a linear combination of the distribution of nonzero stresses (9) and the delta function to account for zero stresses $P(\tilde{\sigma})=C_1P_{nz}(\tilde{\sigma})+(1-C_1)\delta(0)$. The constant C_1 signifies the fraction of nonzero stresses. Then, the mean and the mean square of the stress are as follows:

$$\langle\tilde{\sigma}\rangle=\int_0^\infty \tilde{\sigma}P(\tilde{\sigma})d\tilde{\sigma}=C_1\langle\tilde{\sigma}\rangle_{nz}=1, \tag{13}$$

$$\langle\tilde{\sigma}^2\rangle=\int_0^\infty \tilde{\sigma}^2P(\tilde{\sigma})d\tilde{\sigma}=C_1\sigma_0^2(n+1)(n+2). \tag{14}$$

From the first equation we obtain $C_1=1/\langle\tilde{\sigma}\rangle_{nz}$ and, using (11), we arrive at the following expression for the width of distribution:

$$\text{width}=\sqrt{\sigma_0(n+2)-1}=\sqrt{\sigma_0+\langle\tilde{\sigma}\rangle_{nz}-1}. \tag{15}$$

Expression (15) reduces to $\sqrt{\sigma_0}=(n+1)^{-1/2}$ if zero stresses are absent, i.e., when all sensors register at least one strike per Δt and $\langle\tilde{\sigma}\rangle_{nz}=\langle\tilde{\sigma}\rangle=1$. Here, the width is determined by averaging effects and correlations, as we discuss later. On the other hand, if zero stresses are present, there is a significant dependence of the width on the nonzero stress $\langle\tilde{\sigma}\rangle_{nz}$. In a limiting case $\langle\tilde{\sigma}\rangle_{nz}\gg 1$, appropriate to systems shown in Fig. 11, (15) reads

$$\text{width}=\sqrt{\left(\frac{1}{1+n}+1\right)\langle\tilde{\sigma}\rangle_{nz}-1}\propto\sqrt{\langle\tilde{\sigma}\rangle_{nz}}, \tag{16}$$

where we have used the fact that for $\langle\tilde{\sigma}\rangle_{nz}\gg 1$ sensors do not register more then one particle at a time, and for single particle contacts $n=$const, as explained below. Equation (16) is consistent with visual estimate of the widths in Fig. 11: The larger $\langle\tilde{\sigma}\rangle_{nz}$ (shown in the right top area on each plot), the wider is the distribution. Next we show that $\langle\tilde{\sigma}\rangle_{nz}$ depends on the collision rate, area of the sensors, and averaging time.

Let $N_t=n_sn_T$ be the total number of stress measurements, obtained from all n_s sensors during n_T time intervals. Out of N_t stresses, $N_{nz}\leqslant N_t$ are nonzero. The nonzero average stress depends on the size of sensor A_s and averaging time Δt,

$$\langle\tilde{\sigma}\rangle_{nz}=\frac{\langle\sigma\rangle_{nz}}{\langle\sigma\rangle}=\frac{N_t}{N_{nz}}=\frac{1}{wA_s\Delta t}, \tag{17}$$

where w is the frequency of nonzero stress events per unit area. For low-collision rate with the sensors, when not more than one particle strikes A_s during Δt, w signifies particle-wall collision rate per unit area.

Relations (16) and (17) allow us to explain the distributions in Fig. 11. The sensor areas and averaging times are fixed, so it is the rate of nonzero events w which determines the average and the width. To first approximation $w\propto\nu$ close to the respective boundary. From $\nu(y)$ in Fig. 2 we see that, without oscillations, ν is smaller at the top wall leading to wider distributions. If oscillations are present, ν is smaller at the bottom, so distributions are wider there.

2. Averaging effects

In this section we study one of the factors that can affect the parameter n, i.e., the number of contacts N between the particles and a sensor during the averaging time Δt.

Let us define the parameter n_0 that is characteristic for the distribution of stresses due to single particle contacts,

$$P_N(\tilde{\sigma})=c\tilde{\sigma}^{n_0}e^{-\tilde{\sigma}/\sigma_0},\quad N=1. \tag{18}$$

If more than one particle collide with the sensor of area A_s during time Δt ($N>1$), then the stress distribution is different due to *averaging effects*. For instance, when two particles

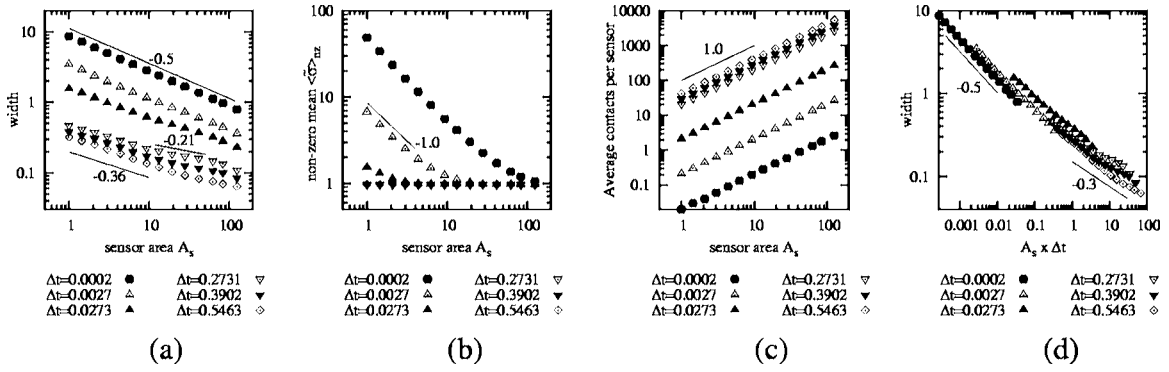

FIG. 12. (a) The widths of force distributions as defined by (12) vs the sensor area A_s (in units of $\langle d\rangle^2$) for various Δt's. (b) Average nonzero stress $\langle\tilde{\sigma}\rangle_{nz}$ as a function of A_s (for $\Delta t \geqslant 0.2731$ $\langle\tilde{\sigma}\rangle_{nz}=1$). (d) Average number of contacts per sensor as a function of A_s. (c) The widths vs $\Delta t A_s$. The solid lines have specified slopes.

strike the same sensor during Δt, $N=2$, the probability of registering total stress F depends on the probability of one of them contributing the stress $\sigma \leqslant F$ and another one the stress $F-\sigma$. Assuming both considered particles have independent distributions (18), the distribution of their collective stress F is $P_2(F)=\int_0^F P(\sigma)P(F-\sigma)d\sigma$. Using (18) and the integral identity

$$\int_0^F \sigma^r (F-\sigma)^q d\sigma = F^{(r+q+1)}\Gamma(r+1)\Gamma(q+1)/\Gamma(r+q+2) \tag{19}$$

valid for any positive real numbers r and q, and, in particular, for $r=q=n_0$, we arrive at the following distribution for the stresses generated by double strikes $P_2(\tilde{F}) = c_2 \tilde{F}^{(2n_0+1)} e^{-\tilde{F}/\sigma_0}$, $\tilde{F}=F/\langle\sigma\rangle$, where c_2 is a normalization coefficient. Applying the same argument to the case when N particles strike the sensor during Δt we obtain the following distribution of stresses:

$$P_N(\tilde{\sigma}) = c\tilde{\sigma}^{[N(n_0+1)-1]} e^{-\tilde{\sigma}/\sigma_0}. \tag{20}$$

The above calculation sets the relation between the parameter n and the number N as $n=N(n_0+1)-1$, see (9). Therefore, if the particles are not correlated, we obtain that the distributions of stresses generated by multiples collisions are characterized by higher power n. We will see below that this result is justified for the results shown in Fig. 11.

This conclusion may be used to explain the increased values of n in Fig. 11(c), bottom, and Fig. 11(d), bottom. Here, the bottom wall is vibrated and most of the stress data are collected during the phase when the bottom is rising up. This phase is characterized by increased compaction of particles close to the sensors and an increased N. However, an increase of N cannot be responsible for the large n's on the top wall shown in Fig. 11(b), and, to a lesser extent, Fig. 11(a), top. In particular regarding Fig. 11(b), we expect that the source of large n lies in the separately verified result that the typical normal components of the velocities of the particles colliding with the top wall are large, leading to different stress distribution.

The results of Fig. 11 allow us to estimate the parameter n_0 defined earlier in this section as the value of n corresponding to the distribution of stresses registered by the sensors with $N=1$. Because $n_0 \leqslant n$ [see (20)], the smallest found n provides an upper bound on n_0. The lowest values of n are found in the distributions shown in Fig. 11: (a) bottom, (b) bottom, (c) top, and (d) top. For these cases $n<1$; therefore, $n_0<1$. This result is very different from $n_0=2$ in the q model: this should be no surprise because q model assumes high volume fraction and static configuration.

3. Correlations

The dependence of the normal stress distributions on the number of contacts per sensor can be described by (20) only when the particles participating in contact with a sensor are not correlated. However, there are certain regimes and conditions of granular flow when this assumption may not be correct. For example, Miller, O'Hern, and Behringer[23] studied the response of the force distribution to the number N, controlled by the size of particles, and found that in dense granular flow the distribution widths were approximately independent of N. This independence was attributed to the presence of correlations due to force chains.

Here we present the systematic study of the effect of sensor size (and, hence, the number N) on the bottom wall stress distributions for our typical configuration without oscillations and with glued particles, Fig. 2(a). This study allows us to confirm the validity of our predictions (15) and (20) in a more quantitative way and to check for possible correlations.

Figure 12(a) shows the results for width (12) as a function of A_s for fixed values of Δt in the range between $T_w/100=0.0002$ sec and $20T_w=0.5463$ sec. This range includes our typical value $\Delta t=T_w/10=0.0027$ sec (open triangles) used to obtain the distributions in Fig. 11. To help interpretation of the results, we plot in Fig. 12(b) the value of $\langle\tilde{\sigma}\rangle_{nz}$, in Fig. 12(c) the average number of contacts per sensor, and in Fig. 12(d) the widths of distributions versus the product of the averaging time and the sensor area.

This figure shows that if zero stresses are present, i.e., $\langle\tilde{\sigma}\rangle_{nz}>1$, the widths scale with the sensor area as $A_s^{-0.5}$, which is the scaling predicted by (16). This result applies to all sensor sizes when $\Delta t=0.0002$ sec, to the sensors of

$A_s < 20\langle d\rangle^2$ when $\Delta t = 0.0027$ sec, and to the sensors of $A_s < 2\langle d\rangle^2$ when $\Delta t = 0.0273$ sec, see Fig. 12(b).

When zero stresses are not present ($\langle\tilde{\sigma}\rangle_{nz} = 1$) the width (15) reduces to

$$\text{width} = \sqrt{\sigma_0} = [N(n_0 + 1)]^{-0.5}. \tag{21}$$

Here $N \propto A_s$ is a number of contacts per sensor from (20) and absence of correlations is assumed. This relation (21) is consistent with the $A_s^{-0.5}$ in Fig. 12(a) in the case $\Delta t = 0.0027$ sec and $A_s > 20\langle d\rangle^2$. However, when $\Delta t \geqslant 0.0273$ sec [for these large Δt's, the zero stresses are absent for almost all considered sensors, see Fig. 12(b)] the widths decrease as A_s is increased at a slower rate than predicted by (21). The slowest decrease, approximately $A_s^{-0.21}$, occurs for the sensor sizes $10\langle d\rangle^2 < A_s < 100\langle d\rangle^2$, and for the averaging times of 0.2731 sec.

We expect that the origin of this slower decrease is the presence of correlations between the particles striking the same sensor (which may include self-correlation, i.e., the same particle colliding with the same sensor on multiple occasions during a given Δt). For example, the distribution of stresses due to N completely correlated particles acting on each sensor would have $n = n_0$, leading to the widths independent of A_s. Therefore, the stronger are the correlations between particles, the lower is the exponent in the width versus A_s plot. In Fig. 12(a) we can see that stronger correlation effects (i.e., slower decrease of the widths with an increase of A_s) occur for longer Δt and larger A_s. This is even more evident when the width is plotted against the product $A_s\Delta t$, see Fig. 12(d): the slope changes gradually from -0.5 for small $A_s\Delta t$ to about -0.3 for large $A_s\Delta t$. The collapse of almost all data on approximately single curve in Fig. 12(d) indicates the fact that the same averaging or correlation effects result if either Δt or A_s is increased by a same factor. Possible exception to this rule are very long Δt's, which we discuss below.

We note that in Ref. 23 evidences were found of strong correlations, since they estimated experimentally the width $\propto A_s^0$ for $\Delta t = 0.0005$ sec and $5\langle d\rangle^2 \leqslant A_s \leqslant 80\langle d\rangle^2$. However, the overall ν of their samples was considerably higher. Therefore, the spatial correlations can be explained if one assumes the normal stress on the bottom wall is applied through the network of *force chains*.[33] In our case, where ν's are smaller, we expect that spatial correlations may arise from statistical fluctuations of the local ν. These fluctuations lead to occasional formation of denser structures of particles, stretched from the top to bottom wall: friction ensures that the lifetime of these formations is relatively long. As in the case of force chains, the dense structures carry more stress than the "free" particles in the "interstructure" space, thus introducing spatial correlations. Unlike the force chains, the dense structures do not form dense force network. They may form and disappear allowing for longer "structure-free" periods. This concept is consistent with the fact that our correlations are weak and detected only when Δt and A_s are large enough to include such a structure event. In addition, the average number of contacts with sensors, see Fig. 12(c), is larger than 10 in the regimes where (21) fails. This fact suggests the possibility of *frequent returning contacts* of the same particle with a sensor, which is a signature of a particle pressed to the sensor from above, as one would expect for a particle that is member of a dense structure. The existence of similar structures (named "transient force chains") was also suggested in Ref. 27.

We note that the dependence of the width on A_s becomes stronger again in the case of very long Δt's, see the results for $\Delta t = 0.5463$ sec in Fig. 12(a). Simple estimate shows that this change in trend occurs when Δt is so long that a particle, moving with a typical velocity, travels across a sensor in the time that is shorter than Δt, therefore decreasing this self-correlating effect.

B. Tangential stress distributions

Figure 13 shows the tangential stress distributions, defined by (7), scaled by mean tangential stress $\tilde{\sigma} = \sigma_t/\langle\sigma_t\rangle$ for the same boundary conditions as discussed in Fig. 11. The average tangential stress, shown on the horizontal labels, is positive at the top wall and negative at the bottom, since the top wall is mostly accelerating the particles while the bottom wall is slowing them down. The absolute value of the average tangential stress $\langle\sigma_t\rangle$ tells us the magnitude of torque and power needed to keep the top wall rotating and the bottom wall stationary. It is considerably larger for the systems with glued particles, since their presence enhances momentum exchange.[10] We also note that $|\langle\sigma_t\rangle|$ is larger on the top wall than on the bottom by a factor of 3 without oscillations, and by a factor of 5 with oscillations. This factor is larger in the latter system, since oscillations increase the vertical velocity fluctuations and the dissipation of the momentum on the sidewalls is increased.

Similar to the normal stresses, we observe the exponential tails for $\tilde{\sigma} > \tilde{\sigma}_0$, where $\tilde{\sigma}_0$ is the location of the peak of a distribution. For most considered cases, these tails have the same slope and location as the tails of the normal stresses, suggesting a strong correlation. However, for $\tilde{\sigma} < \tilde{\sigma}_0$ the tangential stresses differ qualitatively from the normal ones, since the PDFs of tangential stresses allow for stresses of the sign opposite to $\langle\sigma_t\rangle$.

In the case of oscillating bottom wall [Figs. 13(c) and 13(d) bottom panel], the tangential distributions are noticeably wider than the normal stress distribution. This can be explained by noticing that when bottom is moving up, the particles next to the bottom wall are constrained by increased ν to move predominantly in the horizontal directions, therefore increasing fluctuations of tangential stresses.

To confirm more qualitatively the relation between the normal and tangential stresses we study their time series. Consider the time signals $\tilde{\sigma}_n(t)$ and $\tilde{\sigma}_t(t)$. If these signals are correlated, we can write

$$\tilde{\sigma}_t(t) = K\tilde{\sigma}_n(t) + R(t), \tag{22}$$

where $R(t)$ is a noise term such that $\langle R\rangle = 0$ and $K = \langle\tilde{\sigma}_t\rangle/\langle\tilde{\sigma}_n\rangle = 1$. Then the cross-correlation function defined as $C_{nt}(t) = \langle\Delta\tilde{\sigma}_n(t_0)\Delta\tilde{\sigma}_t(t_0+t)\rangle$ must be equal to the autocorrelation function defined as $C_{nn}(t) = \langle\Delta\tilde{\sigma}_n(t_0)\Delta\tilde{\sigma}_n(t_0+t)\rangle$. In the definition of these time-correlation functions, $\Delta\tilde{\sigma} = \tilde{\sigma} - \langle\tilde{\sigma}\rangle$

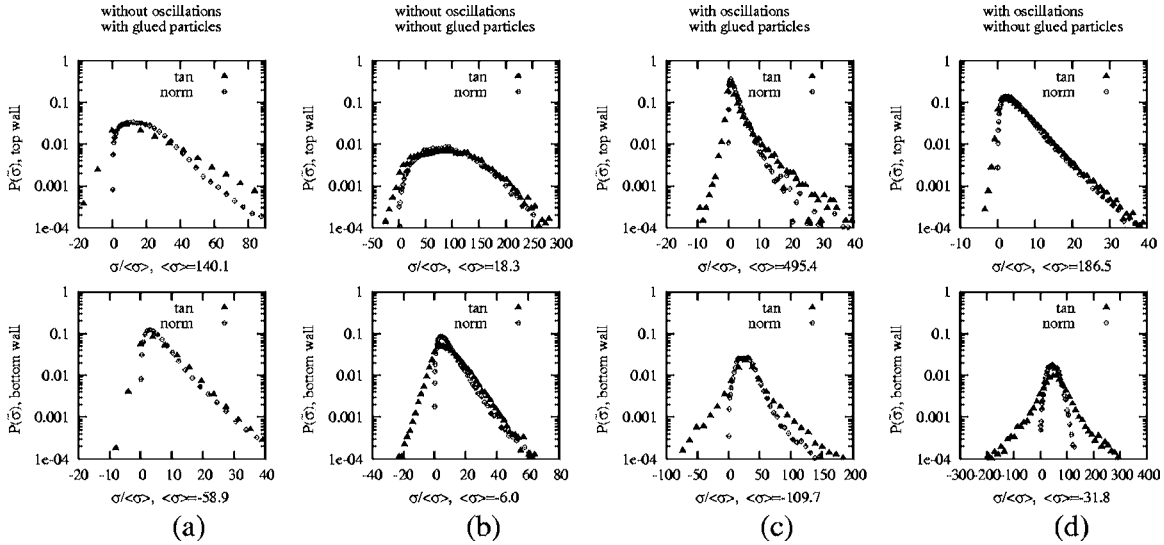

FIG. 13. Log plot of PDF for tangential nonzero stresses (filled triangles) on the top wall (top panel) and on the bottom wall (bottom panel) in the typical configuration with four boundary conditions: (a) and (b) without oscillating bottom wall, (c) and (d) with oscillating bottom wall, (a) and (c) with glued particles, (b) and (d) without glued particles. Average tangential stress per area $\langle\sigma\rangle=\langle\sigma_t\rangle$ is in units of $\rho_s\langle d\rangle^2/\mathrm{sec}^2$. For comparison, normal stress distributions from Fig. 11 are replotted here (open circles).

and averaging is performed over all initial times t_0.

Figure 14 shows that, for the stresses on the bottom wall $C_{nt}\approx C_{nn}$, confirming the relation (22) with $\langle R\rangle=0$. Also, we see that the correlation functions decay very fast within an interval shorter than averaging time. For longer times, the correlation function is small but still noticeable. We note that larger particle velocities lead to faster decay of correlation functions in Fig. 14(a) compared to 14(b) [see also Figs. 2(a) and 2(b)].

The results of this section confirm strong correlation between the normal and tangential stresses. This correlation renders that the conclusions obtained for normal stresses also apply to the tangential stresses.

V. CONSTANT VOLUME VERSUS CONSTANT PRESSURE SIMULATIONS

All the results we have discussed so far are obtained for the systems characterized by prescribed volume dependence on time. We refer to these cases as *controlled volume* simulations, with constant volume (CV) simulations being the special case. It is, however, well known that the volume constraint can affect significantly the granular flow. The system can be easily locked in a jammed state. That is why dense sheared granular flow experiments, such as flow in a Couette cell,[23] or gravity-driven flows down an incline,[34,35] are commonly carried out using controlled pressure. Recently, new studies emerged that indicated the importance of the difference between controlled-volume and controlled-pressure boundary conditions. For example, Aharonov and Sparks[36,37] use 2D numerical simulations to study the response of the dense sheared granular system to the applied boundary pressure, finding different shearing modes for very similar ν's.

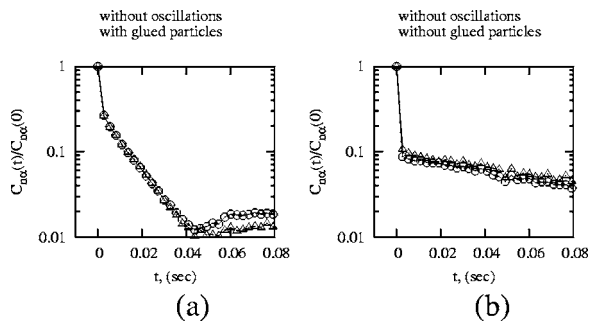

FIG. 14. Scaled stress autocorrelation (circles) and cross-correlation (triangles) functions for the stresses on the bottom wall in the systems without oscillations. (a) With glued particles. (b) Without glued particles.

Therefore, now we concentrate on constant pressure (CP) setup. In laboratory experiments the CP condition can be realized by setting a movable (say, bottom) wall, on a compressed spring.[20] Any increase of the pressure inside the cell results in an increase of the volume of the cell and vice versa. The compressed spring realization is especially relevant if the experiment is conducted in zero gravity.

In numerical simulations we adopt the following algorithm (an approximation of a compressed string) to control the pressure. The whole time span of simulation is divided into small time intervals $\Delta\tau$. At the beginning of each time interval we calculate the total stress on the bottom wall, σ, using (6) with $A_s=A_{\mathrm{base}}$ and put $\Delta t=\Delta\tau$. We then compute the vertical velocity of the bottom wall, v_b, as follows:

$$v_b=\begin{cases}-\bar{v}_b, & \sigma>\bar{\sigma}+\delta\sigma/2,\\ 0, & \bar{\sigma}-\delta\sigma/2<\sigma<\bar{\sigma}+\delta\sigma/2,\\ +\bar{v}_b, & \sigma<\bar{\sigma}-\delta\sigma/2,\end{cases} \tag{23}$$

where $\bar{\sigma}$, $\delta\sigma$, and v_b are the prescribed stress, stress tolerance, and velocity of the bottom wall. Within each time interval $\Delta\tau$ we run the controlled volume simulations with constant velocity of the bottom wall given by (23). The resulting changes of the volume of the cell adjust the stress back to the prescribed value, leading to CP conditions. We

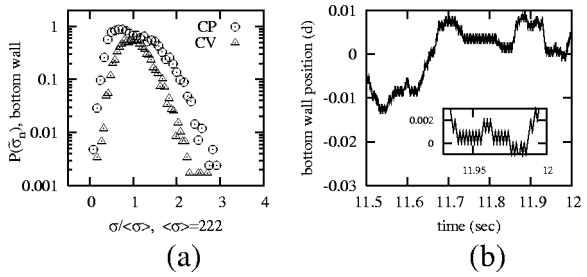

FIG. 15. (a) Stress on the base PDF in CP case (circles) compared to CV (triangles). Here $\Delta t=\Delta\tau=T_w/25$ and $A_s=A_{\text{base}}$. (b) The position of the bottom wall (in units of $\langle d\rangle$) in the CP simulations. Zero corresponds to the mean position of the wall. Inset: same data on finer time scale.

note that this model leads to vibration of the bottom wall in steady state, similarly to experiments.[38]

We consider the system without oscillations and with glued particles on the top wall [Fig. 2(a)] as a basis for all our CP simulations, and set the constant stress on the bottom wall being equal to the average stress $\langle\sigma_n\rangle$ on this wall that we measured in CV simulations with $\Omega=10$ rad/sec. The choice of the parameters used in the model (23) is

$$\bar{\sigma}=222\rho_s\langle d\rangle^2(\text{sec}^{-2}),\quad \delta\sigma=20\rho_s\langle d\rangle^2(\text{sec}^{-2}), \tag{24}$$

$$\Delta\tau=T_w/25,\quad \bar{v}_b=\langle d\rangle/\Delta\tau/1000=0.915\langle d\rangle/\text{sec}. \tag{25}$$

Figure 15(a) shows the PDF for the stresses on the complete bottom wall using the parameters (24) and (25) and $\Delta t=\Delta\tau$. For comparison, the results of CV simulations for the same A_s and Δt are also shown. We see that the CP distribution is wider compared to CV case. To understand this difference it is useful to distinguish three sets of collected stress data in CP setting, each set resulting from one of three phases of the bottom wall motion: moving up, staying put, and moving down (this separation of the stresses is possible only because $\Delta t=\Delta\tau$, i.e., during the averaging time the bottom wall does not change its velocity). The resulting CP distribution corresponds to the superposition of these three phases, leading to widening of the stress distribution in CP setup, which can be estimated as follows. If $\Delta v_y^{(\text{CV})}$ is a change in the normal component of velocity of a particle interacting with a stationary sensor and $\Delta v_y^{(\text{CP})}$ is a change in the normal component of the velocity of the same particle interacting with a sensor that has the velocity v_b, then $\Delta v_y^{(\text{CP})}=\Delta v_y^{(\text{CV})}+v_b$. If we have N particles of average diameter $\langle d\rangle$ interacting with a sensor A_s during Δt then, using the definition (6),

$$\sigma_n^{(\text{CP})}=\sigma_n^{(\text{CV})}+K_1\frac{Nv_b}{A_s\Delta t}, \tag{26}$$

where $\sigma_n^{(\text{CP})}$ is a stress on a moving sensor, $\sigma_n^{(\text{CV})}$ is a stress on a stationary sensor, and $K_1=\pi\rho_s\langle d\rangle^3/6$. Therefore, one expects that the distribution of $\sigma_n^{(\text{CP})}$ is $\approx 2K_1Nv_b/(A_s\Delta t)$ wider than the distribution of $\sigma_n^{(\text{CV})}$. This argument predicts that $(\text{width}^{(\text{CP})}-\text{width}^{(\text{CV})})/\text{width}^{(\text{CV})}\sim 0.1-0.2$, consistently with the results shown in Fig. 15(a) [in the estimate we use $N=10$, based on the results shown in Fig. 12(c)]. We note that the above argument applies only to the normal stresses, since this is the direction of v_b.

In principle, both normal and tangential stresses can also be affected by the changes in ν and in the velocity profiles due to the motion of the bottom wall, see Fig. 15(b). To estimate this effect, we note that it is characterized by the approximate frequency of $1/(2\Delta\tau)=457$ Hz and the amplitude of $\bar{v}_b\Delta\tau/2=0.0005\langle d\rangle$. Despite high frequencies, the vibrations of such a small amplitude are not expected to significantly modify stress distributions, as also illustrated by Fig. 16.

Figure 16 shows stress PDFs on typical size sensors using our typical averaging time $\Delta t=T_w/10$. Compared to the stresses in CV simulations, Figs. 11(a) and 13(a), we do not see any significant differences. This is because $\Delta t>\Delta\tau$; therefore, during the averaging time the velocity of the bottom wall can change once or twice, resulting in "averaging out" the effect of the bottom wall motion. Therefore, we conclude that the model specified by (23)–(25) is effective in keeping constant stress, while not modifying significantly stress distributions on the time scales of interest.

Bagnold scaling

In this section we investigate the effect of the shearing velocity Ω on the stresses. The relation between average normal stress and Ω under certain conditions takes the form of *Bagnold scaling*,[39] where stresses increase with the square of the shear rate.[3,21,34,38,40] This quadratic dependence is observed for the granular flows at high shearing rates or for lower ν's, i.e., in the systems where particles are not involved in multiple elastic deformations.[41]

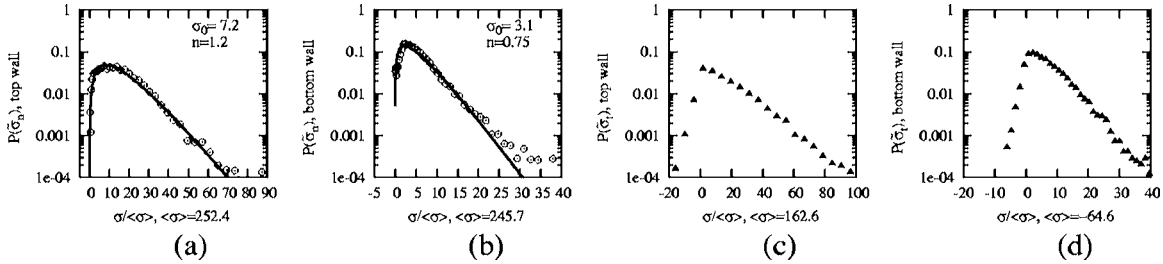

FIG. 16. Constant-pressure simulations: Stresses for the case without oscillations and with glued particles on the top wall. Size of sensors $d_s=1.09\langle d\rangle$. (a) and (c) Sensors are on the top wall; (b) and (d) sensors are on the bottom wall; (a) and (b) normal stress PDF; (c) and (d) tangential stress PDF.

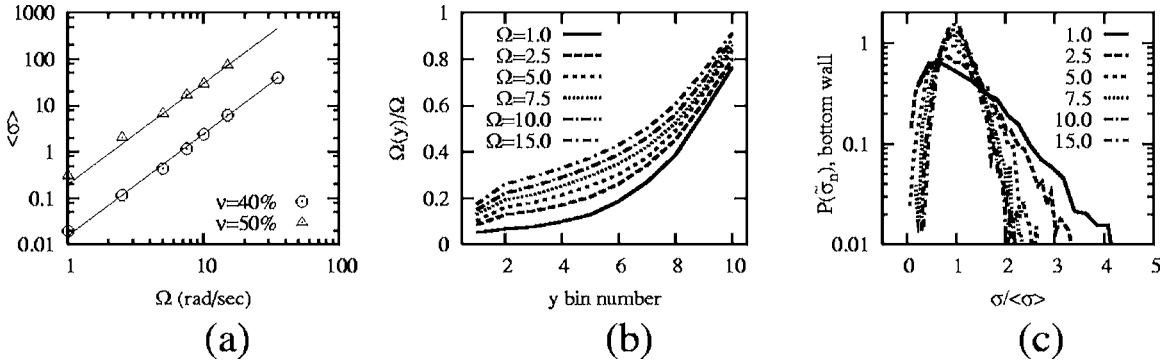

FIG. 17. CV simulations. (a) Stress as a function of Ω in log-log plot. Circles: $\nu=40\%$. Triangles: $\nu=50\%$. Solid lines are the best fits (see text). The rest of results shown are calculated using $\nu=40\%$. (b) Velocity profiles; (c) stress PDF, bottom wall, $\Delta t=T_w/25$. Measurements are taken over $\Delta T=5000\Delta t=5.47$ sec except for $\Omega=1$ rad/sec, where $\Delta T=2$ sec.

Figure 17(a) shows log-log plot of the mean normal stresses on the bottom wall versus Ω at CV setting for the system shown in Fig. 2(a). For configurations of $\nu=40\%$ and $\nu=50\%$ these results confirm Bagnold scaling for the range of Ω's between 1 rad/sec and 35 rad/sec. The data are fitted by the power function $\langle\sigma\rangle=a\Omega^b$ with $a=0.015$ and $b=2.20\pm0.2$ for $\nu=40\%$ and $a=0.201$ and $b=2.18\pm0.2$ for $\nu=50\%$.

Figure 17(b) shows scaled velocity profiles for different Ω's in CV simulations. The profiles are higher for faster shearing. The origin of this dependence may be related to the effect of sidewalls on the sheared system. Indeed, when we shear the system with elastic and smooth sidewalls, see Fig. 4, the profiles do not depend on Ω. Experimental studies[42] also confirm the independence of velocity profiles on Ω if boundary effects are significantly minimized. To explain these results we consider the dependence of restitution parameters on the particle's velocity in particle-sidewall interactions. The normal coefficient of restitution (4) depends on the normal velocity of colliding particle; however, this velocity is not influenced significantly by Ω. On the other hand, the coefficient of tangential restitution, β, in the case of sliding contacts (5) depends stronger on Ω, since it involves the ratio of normal to tangential velocity, and the latter scales with Ω. As it can be seen from (4), lower ratio has the same effect on dissipative mechanics as lower coefficient of friction, μ. Therefore, in the case of higher shear rates, the effect of sidewalls on the granular flow is reduced, explaining the velocity profiles in Fig. 17(b). Stresses shown in Fig. 17(c) are discussed below in the context of comparative study of CV and CP.

In CP simulations we choose the fixed value of the stress on the bottom wall given by (24). Figure 18(a) shows the vertical position of the bottom wall h as a function of time for different Ω ($h=0$ corresponds to $\nu\approx40\%$). As expected, we see that slower/faster shearing leads to smaller/larger stress, and to an adjustment of the wall position. The stabilized (long time) wall positions are used to calculate ν for each Ω, shown in Fig. 18(b). We note significant change in ν as Ω is modified: ν at high shearing (35 rad/sec) is about 1.6 times smaller than ν at low shearing (1 rad/sec).

Figure 19(a) shows the effect of Ω on the velocity profiles. For small Ω's, $\Omega\leqslant2.5$ rad/sec, the shearing is stronger for larger Ω. For intermediate Ω's, $2.5\ \text{rad/sec}\leqslant\Omega\leqslant5$ rad/sec the velocity profiles are almost the same, and for $\Omega\geqslant5$ rad/sec the shearing decreases with an increase of Ω. These results can be understood in terms of volume fraction as a determining factor. For the smallest Ω [solid line in Fig. 19(a)] ν is about 53%; therefore, local jammed areas can be formed inside the sample reducing the overall mobility and shearing. These jammed areas can manifest themselves as "plateaus" in velocity profile. One such plateau can be seen in Fig. 19(a), solid line, for $4<y<5$. As ν decreases with an increase of Ω, the sample gets more fluidized and the shear-

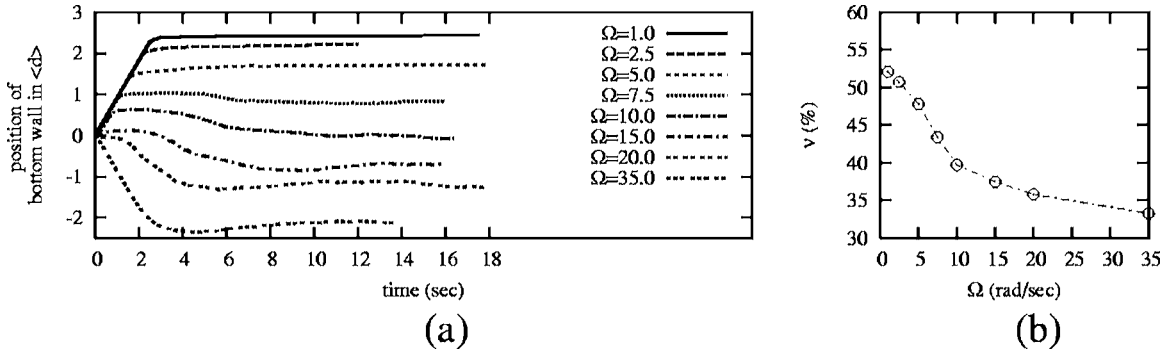

FIG. 18. Constant-pressure simulations. (a) Position of the bottom wall h (in units of $\langle d\rangle$) as a function of time for different shearing velocities; (b) ν as a function of Ω.

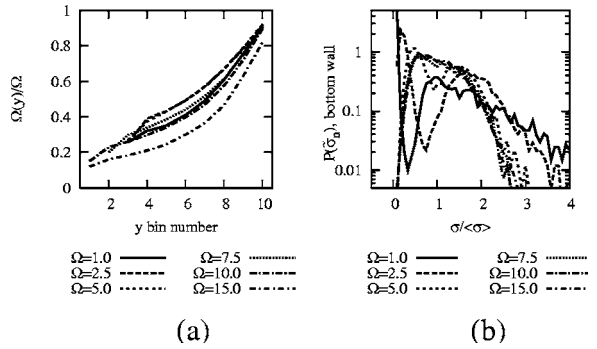

FIG. 19. CP simulations. (a) Velocity profiles; (b) stress PDF, bottom wall. These distributions are obtained from the stress data taken every $\Delta t=\Delta\tau=T_w/25$ sec over $\Delta T=5000\Delta t$.

ing improves. However, further increase of Ω and decrease of ν makes the system more "compressible:" the dilation close to the top wall is stronger, reducing the momentum flux from the top wall to the bulk of the sample, resulting in weaker shearing. Therefore, the influence of Ω on a CP system is more complicated than in a CV case, where velocity profiles are changing monotonously with Ω, see Fig. 17(b).

The distributions of the normal stress on the bottom wall are shown in Fig. 17(c) for the CV and in Fig. 19(b) for the CP. In both cases, the widths of distributions increase with a decrease of Ω. The distributions differ in the following: in the CP case [Fig. 19(b)] the distribution shows a double peak at low shearing, which is absent in the CV case. This double peak occurs, since at low Ω, ν is high, up to 52%. Thus the collision rate between the particles and the moving bottom wall is higher, and hence larger momentum is transferred to the granular system. If this momentum is large enough, we have the situation in which the "restoring force" of the bottom wall brings the system in just one interval $\Delta\tau$ from the overstressed state to understressed state or vice versa. Therefore, velocity of the wall, (23), alternates between positive and negative without taking zero value, resulting in two peaks in stress distribution: one for overstressed state and another one for understressed state.

VI. CONCLUSIONS

The presented studies concentrate on 3D event-driven simulations in the Couette geometry with top rotating wall and with physical boundary conditions in zero gravity. The velocity and volume fraction distributions are strongly dependent on various boundary conditions, such as top shearing wall properties, sidewall properties, presence of oscillations of the bottom wall, or intensity of shearing. The overall volume fraction of studied granular system is 40%; however, the shearing and vibrating walls impose the nonuniformity in volume fraction distribution with the formation of high-dense band (cluster) where local volume fraction reaches up to 60%. The cluster can respond to shearing in different ways. For example, while very rough and inelastic top wall, but without glued particles, cannot induce any significant shearing when sidewalls are dissipating, it imposes a shear and high tangential velocities of all particles in the case of smooth and elastic sidewalls. Typically, inside the cluster the shear rate is very small. However, the presence of the glued particles on the top wall considerably increases shear rate inside this cluster.

The presence of oscillations of the bottom wall seems to have three effects: (1) The slippage velocity at the bottom increases. (2) The dense cluster is located further away from the bottom wall compared to the systems without oscillations. (3) Equilibrating times to reach a steady state are shorter in the systems with oscillations due to the increased collision rate.

The equilibrating dynamics involves attaining the steady-state values of volume fractions and velocities. The time scales of these two equilibrating processes are different: in most cases, steady-state profile in volume fraction is attained very fast, while velocity profiles reach their final shape much later. However, the volume fraction distribution takes longer to reach a steady state when the rate of energy input is low. This occurs in the systems without glued particles and without oscillations. For example, in the so-called "delayed dynamics" regime, described in Sec. III B, the time needed for the cluster to accumulate enough energy to disattach from the bottom wall can be very long. However, once this happens, the velocity profile changes drastically. More generally, these simulations show that the velocities and volume fractions strongly depend on boundary conditions: simulations using, e.g., periodic boundary conditions may miss a number of interesting effects presented in this work.

We have also analyzed stress and stress fluctuations on the boundaries. We find that the distribution of normal stresses in a system of 40% volume fraction and rapid granular flow can be described by the same functional form (9) as used for stress distribution in static dense system, i.e., with power-law increase for small stresses and exponential decrease for large ones. Considering this functional form as a useful guide, we predict the behavior of main characteristics of stress distributions as a function of sensor area and averaging time. These predictions describe well the width of distributions for small sensors and short Δt's. However, they fail for large sensors and long averaging times, suggesting the existence of additional correlations not accounted by our functional form. The correlations may be related to the existence of "denser structures" in the simulated systems.

We simulate constant pressure boundary condition and discuss the differences between the results in constant volume and constant pressure settings. A key observation here is very different response to an increase of shearing velocity in the system with constant-pressure boundary condition compared to the systems with constant-volume boundary condition. In the first case the shearing velocities are increasing because of the velocity dependence of the coefficients of restitution while in the second case they are initially increasing and then decreasing because of the changes of volume fraction with imposed shear.

ACKNOWLEDGMENTS

The authors acknowledge the support of NASA, Grant No. NNC04GA98G, and thank Robert P. Behringer and

Karen E. Daniels of Duke University and Allen Wilkinson of NASA Glenn for very useful discussions.

[1] J. T. Jenkins and S. B. Savage, "A theory for the rapid flow of identical, smooth, nearly elastic, spherical particles," J. Fluid Mech. **130**, 187 (1983).
[2] C. K. K. Lun, S. B. Savage, D. J. Jeffrey, and N. Chepurniy, "Kinetic theories for granular flow: Inelastic particles in Couette flow and slightly inelastic particles in a general flowfield," J. Fluid Mech. **140**, 223 (1984).
[3] C. S. Campbell and C. E. Brennen, "Computer simulation of granular shear flows," J. Fluid Mech. **151**, 167 (1985).
[4] C. S. Campbell and A. Gong, "The stress tensor in a two-dimensional granular shear flow," J. Fluid Mech. **164**, 107 (1986).
[5] L. Bocquet, W. Losert, D. Schalk, T. C. Lubensky, and J. P. Gollub, "Granular shear flow dynamics and forces: Experiment and continuum theory," Phys. Rev. E **65**, 011307 (2002).
[6] J. T. Jenkins and M. W. Richman, "Boundary conditions for plane flows of smooth, nearly elastic, circular disks," J. Fluid Mech. **171**, 53 (1986).
[7] M. Y. Louge, J. T. Jenkins, and M. A. Hopkins, "Computer simulations of rapid granular shear flows between parallel bumpy boundaries," Phys. Fluids A **2**, 1042 (1990).
[8] M. Y. Louge, "Computer simulations of rapid granular flows of spheres interacting with a flat, frictional boundary," Phys. Fluids **6**, 2253 (1994).
[9] K. Hui, P. K. Haff, J. E. Ungar, and R. Jackson, "Boundary conditions for high-shear grain flows," J. Fluid Mech. **145**, 223 (1984).
[10] G. M. Gutt and P. K. Haff, "Boundary conditions on continuum theories of granular flow," Int. J. Multiphase Flow **17**, 621 (1991).
[11] M. Alam and P. R. Nott, "Stability of plane Couette flow of a granular material," J. Fluid Mech. **377**, 99 (1998).
[12] P. R. Nott, M. Alam, K. Agrawal, R. Jackson, and S. Sundaresan, "The effect of boundaries on the plane Couette flow of granular materials: A bifurcation analysis," J. Fluid Mech. **397**, 203 (1999).
[13] B. D. Lubachevsky, "How to simulate billiards and similar systems," J. Comput. Phys. **94**, 255 (1991).
[14] S. Luding, "Granular materials under vibration: Simulations of rotating spheres," Phys. Rev. E **52**, 4442 (1995).
[15] S. F. Foerster, M. Y. Louge, H. Chang, and K. Allia, "Measurements of the collision properties of small spheres," Phys. Fluids **6**, 1108 (1994).
[16] W. Goldsmith, *Impact, The Theory and Physical Behavior of Colliding Solids* (Arnold, London, 1964).
[17] T. Schwager and T. Pöschel, "Coefficient of normal restitution of viscous particles and cooling rate of granular gases," Phys. Rev. E **57**, 650 (1998).
[18] C. Bizon, M. D. Shattuck, J. B. Swift, W. D. McCormick, and H. L. Swinney, "Patterns in 3D vertically oscillated granular layers: Simulation and experiment," Phys. Rev. Lett. **80**, 57 (1998).
[19] O. R. Walton, in *Particulate Two-Phase Flow*, edited by M. C. Roco (Butterworth, Boston, 1993), p. 884.
[20] K. E. Daniels and R. P. Behringer (private communications).
[21] S. B. Savage and D. J. Jeffrey, "The stress tensor in a granular flow at high shear rates," J. Fluid Mech. **110**, 255 (1981).
[22] S. B. Savage, "Analyses of slow high-concentration flows of granular materials," J. Fluid Mech. **377**, 1 (1998).
[23] B. Miller, C. O'Hern, and R. P. Behringer, "Stress fluctuations for continously sheared granular materials," Phys. Rev. Lett. **77**, 3110 (1996).
[24] C. Thornton, "Force transmission in granular media," Kona **15**, 81 (1997).
[25] F. Radjai, M. Jean, J. J. Moreau, and S. Roux, "Force distribution in dense two-dimensional granular systems," Phys. Rev. Lett. **77**, 274 (1996).
[26] S. N. Coppersmith, C. Liu, S. Majumdar, O. Narayan, and T. A. Witten, "Model for force fluctuations in bead packs," Phys. Rev. E **53**, 4673 (1996).
[27] E. Longhi, N. Easwar, and N. Menon, "Large force fluctuations in a flowing granular medium," Phys. Rev. Lett. **89**, 045501 (2002).
[28] D. M. Mueth, H. M. Jaeger, and S. R. Nagel, "Force distribution in a granular medium," Phys. Rev. E **57**, 3164 (1998).
[29] C. Liu, S. R. Nagel, D. A. Schecter, S. N. Coppersmith, S. Majumdar, O. Narayan, and T. A. Witten, "Force fluctuations in bead packs," Science **269**, 513 (1995).
[30] M. L. Nguyen and S. N. Coppersmith, "Properties of layer-by-layer vector stochastic models of force fluctuations in granular materials," Phys. Rev. E **59**, 5870 (1999).
[31] J. E. S. Socolar, "Average stresses and force fluctuations in non-cohesive granular materials," Phys. Rev. E **57**, 3204 (1998).
[32] S. F. Edwards and D. V. Grinev, "Statistical mechanics of granular materials: Stress propagation and distribution of contact forces," Granular Matter **4**, 147 (2003).
[33] D. Howell and R. P. Behringer, "Fluctuations in a 2D granular Couette experiment: A critical transition," Phys. Rev. Lett. **82**, 5241 (1999).
[34] L. E. Silbert, D. Ertas, G. S. Grest, T. C. Halsey, D. Levine, and S. J. Plimpton, "Granular flow down an inclined plane: Bagnold scaling and rheology," Phys. Rev. E **64**, 051302 (2001).
[35] M. Y. Louge and S. C. Keast, "On dense granular flows down flat frictional inclines," Phys. Fluids **13**, 1213 (2001).
[36] E. Aharonov and D. Sparks, "Shear profiles and localization in simulations of granular materials," Phys. Rev. E **65**, 051302 (2002).
[37] E. Aharonov and D. Sparks, "Rigidity phase transition in granular packings," Phys. Rev. E **60**, 6890 (1999).
[38] S. B. Savage and M. Sayed, "Stresses developed by dry cohesionless granular materials sheared in an annular shear cell," J. Fluid Mech. **142**, 391 (1984).
[39] R. A. Bagnold, "Experiments on a gravity-free dispersion of large solid spheres in a Newtonian fluid under shear," Proc. R. Soc. London, Ser. A **225**, 49 (1954).
[40] G. Bossis, Y. Grasselli, and O. Volkova, "Granular rheology in zero gravity," J. Phys.: Condens. Matter **16**, 3279 (2004).
[41] C. S. Campbell, "Granular shear flows at the elastic limit," J. Fluid Mech. **465**, 261 (2002).
[42] W. Losert, L. Bocquet, T. C. Lubensky, and J. P. Gollub, "Particle dynamics in sheared granular matter," Phys. Rev. Lett. **85**, 1428 (2000).